

Spontaneous creation and annihilation dynamics and strain-limited stability of magnetic skyrmions

Frederic Rendell-Bhatti^{1*}, Raymond J. Lamb¹, Johannes W. van der Jagt², Gary W. Paterson¹, Henk J. M. Swagten² and Damien McGrouther¹

¹SUPA, School of Physics and Astronomy, University of Glasgow, Glasgow G12 8QQ, UK

²Department of Applied Physics, Eindhoven University of Technology, 5612 AZ Eindhoven, The Netherlands

f.rendell.1@research.gla.ac.uk

Magnetic skyrmions are topological magnetic spin structures exhibiting particle-like behaviour. They are of strong interest from a fundamental viewpoint and for application, where they have potential to act as information carriers in future low-power computing technologies. Importantly, skyrmions have high physical stability because of topological protection. However, they have potential to deform according to their local energy environment. Here we demonstrate that, in regions of high exchange energy density, skyrmions may exhibit such extreme deformation that spontaneous merging with nearest neighbours or spawning new skyrmions is favoured to attain a lower energy state. Using transmission electron microscopy and a high-speed imaging detector, we have observed dynamics involving distinct configurational states, in which transitions are accompanied by spontaneous creation or annihilation of skyrmions. These observations raise important questions regarding the limits of skyrmion stability and topological charge conservation, while also suggesting a means of control of skyrmion creation and annihilation.

Skyrmions were originally proposed as a soliton model of the nucleon by Tony Skyrme in 1962¹, but they have since been observed as emergent topological quasiparticles in a variety of condensed matter systems including superconductors², liquid crystals³ and magnetic thin films⁴. Although the specific microscopic mechanisms leading to the formation of skyrmion structures differ in each case, the emergent topological structures bear many similarities and skyrmions are therefore of fundamental interest. Topology defines the distinctness of the geometries in continuous systems such as vector fields, as the inability to continuously map one such system to another. Skyrmions can be understood as localised topological “knots” within continuous fields that cannot be unwound without a discontinuous break in their structure. This property is fundamental to the idea of topological protection, equipping skyrmions with a degree of stability against perturbations and contributing to the description of skyrmions as quasiparticles. Skyrmions can be categorised according to the topological charge defined by their structure, whereby processes in which they participate are expected to obey topological charge conservation. Understanding the “real-world” physical stability and possible interactions of these topological structures is of great importance, especially in magnetic thin films, in which magnetic skyrmions are expected to play a role in future low power computing technologies⁵.

In non-centrosymmetric helimagnetic materials, such as B20 FeGe, the lack of inversion symmetry in the crystal structure, combined with strong spin-orbit coupling gives rise to competition between the Dzyaloshinskii–Moriya interaction (DMI) and the Heisenberg exchange interaction⁶. Owing to this competition, materials with a significant DMI will host a helical magnetic ground state, defined by continuously rotating magnetisation along a particular direction with an associated helical wavevector⁷. It is possible to describe the emergence of a hexagonal magnetic skyrmion lattice crystal (SkX) as a magnetic phase transition involving the nucleation of discrete topological quasiparticles from the helical ground state under favourable conditions of magnetic field and temperature⁸. The description of skyrmions as particle-like objects is supported by experimental observations that indicate their high stability⁹ and their ability to organise themselves into domains within a SkX¹⁰ (as commonly seen in atomic systems) or even “microcrystals” analogous to colloidal crystallisation¹¹. Additionally, the inherent rigidity of individual skyrmions allows current-induced propagation via spin-transfer torque without destruction¹². It has been reported that the transition of a SkX into the topologically trivial ferromagnetic state (high field) or helical state (low field) involves magnetic singularities known as Bloch points that fulfil topological charge conservation during these transitions^{13,14}. However, owing to the extreme difficulties associated with performing nanometre resolved magnetic imaging of a stochastic dynamic process taking place in the range of durations from nanoseconds to tens of microseconds, it remains to be experimentally determined whether topological charge is conserved during skyrmion annihilation processes.

Here, we report the direct observation of spontaneous, repeatable creation and annihilation of individual skyrmions in FeGe using Lorentz transmission electron microscopy and a high-speed imaging detector with a temporal resolution of 10 ms (see Methods for details). Creation and annihilation processes occurring on timescales of tens of milliseconds were observed as a repeated lateral skyrmion motion, captured (Supplementary Video 1) across a SkX domain boundary separating lattice domains (Fig. 1a). These thermally driven transitions involved a number of configurational states with distinct lifetimes, separated by relative energy barriers and characterised by skyrmions of five- and seven-fold coordination (5-7 defects). Aided by micromagnetic simulations, we show that these transitions occur in regions of localised high energy density, dominated by exchange energy, while the wider SkX remains in the stable ground state under conditions of constant applied field and temperature. Furthermore, the observed transitions involved discrete changes in topological charge and we propose that extreme deformation of key skyrmions leads to the emergence and subsequent destruction of antiskyrmions, fulfilling topological charge conservation. This demonstrates an example of magnetic strain-limited stability for skyrmions and suggests that topological protection may be overcome through the spontaneous emergence of topological structures that provide lower energy pathways for skyrmion creation or annihilation.

Identification and characterisation of configurational states

Transitions between six unique configurational states (Fig. 1b–g) were observed within the region defined by the dashed box in Fig. 1a. These states are further categorised into three primary states, namely, P₁, P₂ and P₃ (Fig. 1b–d), and three transition states, namely, T₁, T₂ and T₃ (Fig. 1e–g). Each of the identified states features a lattice defect

structure composed of skyrmions of five- and seven-fold coordination (5–7 defects), highlighted in Fig. 1b by the conjoined pentagon and heptagon, structurally analogous to the 5–7 defects found in graphene¹⁵. Note, only the overall outline of the 5–7 defect is shown in later images. The skyrmions at the centre of the pentagons and heptagons, herein denoted as SkCoP and SkCoH, respectively, differ structurally from regular lattice skyrmions which possess hexagonal symmetry¹⁶ by being more spatially compressed (under five-fold coordination) or expanded (under seven-fold coordination)¹⁷. The motion of the 5–7 defects changes the position of the domain boundary (shown by the blue/red/green dotted lines in Fig. 1a) and is accompanied by very slight shifts in the regular lattice skyrmions in the immediate vicinity as they accommodate the change.

In order to analyse the order of occurrence, each frame was assigned to one of the observed P_x or T_x states (see Methods for details). A portion of this sequence data can be seen in Fig. 1h. The system was observed to transition reversibly between P_x states via T_x states, an example of the reversibility of the transitions is recorded in section J of Fig. 1h. However, some P_x – P_x transitions observed did not visibly appear to proceed via a T_x state (see section K in Fig. 1h). In these cases, we assume that, owing to its short-lived nature compared to the frame acquisition time, occupation of the T_x state simply comprised a small fraction of the duration of an individual frame. Evidence for such an assumption comes from observations in which some smearing of intensity suggested multiple states (P_x and T_x) being captured in a single frame and will be discussed further below. Furthermore, the system did not always transition between different P_x states, as recorded in section L of Fig. 1h. This pattern suggests that, once the system is in a T_x state it can lower its energy by transitioning to a neighbouring P_x state or back to its starting P_x state. Additionally, the observed symmetry of transition probabilities (Fig. 3c) suggests that the system does not randomly transition between the six states but rather hops between adjacent P_x states via the appropriate T_x state. Finally, we describe these transitions in terms of skyrmion creation and annihilation. During P_x to T_x transitions, a SkCoP is created, appearing to be formed by the division of an expanded skyrmion of seven-fold coordination, SkCoH. Conversely, in a T_x to P_x transition, a skyrmion of five-fold coordination, SkCoP, is annihilated by merging with a nearest-neighbour skyrmion. Thus, skyrmion creation is associated with P_x to T_x transitions, and skyrmion annihilation is associated with T_x to P_x transitions, therefore T_x states have a higher local skyrmion density than P_x states.

The precise structure of the skyrmions within the 5–7 defects is elucidated through the spatial analysis of the six observed states. A series of four successive frames of the P_1 state (Fig. 2a) shows that the SkCoH appears to have distinct curvature around its centre and that this curvature increases as the sequence progresses. This behaviour demonstrates the dynamic nature of the SkCoH structure, in which the skyrmion appears to be deforming between elongated and dumbbell structures. Such structures represent a significant deformation from the regular hexagonally coordinated lattice skyrmions. Each pair of images in Fig. 2b consists of a summed intensity image across all observed examples of the state (left) and a Delaunay triangulation analysis of the average skyrmion positions based on their geometric centre of mass (right). In Fig. 2c,d, integrated intensity profiles (extracted from the dotted box in each summed intensity image in Fig. 2b) are plotted. They record the intensity values along a path joining two skyrmions of regular six-fold coordination, passing through a SkCoH in the case of P_x states (Fig. 2c) or through a SkCoP in the case of T_x states (Fig. 2d).

A key feature of the P_x states is the relatively deformed structure of the SkCoH in the 5–7 defect (Fig. 2b). From the summed intensity images, the deformed structure appears to possess the aforementioned dumbbell shape on average. This observation is supported by the intensity profiles in Fig. 2c, which show additionally that the SkCoH in each of the P_x states has a highly similar form. The intensity profiles are characterised by two clearly defined central intensity peaks of approximately equal height, with an intensity 60%–70% that that of regular neighbouring skyrmions of six-fold coordination, and spatial extent double that of regular neighbouring skyrmions of six-fold coordination. Figure 2c also shows that the same-row nearest-neighbour distances (i.e., from the intensity peaks of the SkCoH dumbbell to the intensity peaks of the adjacent regular hexagonally coordinated skyrmions) approximately match those of the bulk lattice: 80 nm. By comparing the SkCoH structure of the two most common states (P_1 and P_2), it was observed that 41% (205 of 499 frames showing P_1) and 87% (328 of 376 frames showing P_2) were characterised by a SkCoH skyrmion possessing an intensity central double peak, as described for the summed intensity images in Fig. 2b. This observation suggests that the precise structure of the SkCoH fluctuates, but a common state (indeed the most common state for the less stable P_2 state) is the dumbbell-like form.

Following a similar set of analyses for the T_x states, the SkCoP in the 5–7 defect appears to be less well defined in the summed intensity images appearing somewhat smeared (Fig. 2b). The intensity profiles in Fig. 2d across the three skyrmions involved show three defined intensity peaks, with a central peak intensity approximately 75%–90% that of the neighbouring peaks. Between their positions, the intensity decreases to around 58%–68% of the central peak values, highlighting the transient nature of the T_x states. The compressed nature of the SkCoP in the T_x state can also be observed in both the Delaunay triangulation map of Fig. 2b and in the intensity profile of Fig. 2d, in which same-row nearest-neighbour distance is measured to be 64 nm, 20% closer than in the bulk lattice. Fresnel (defocused) Lorentz transmission electron microscope (TEM) imaging, while providing high-contrast imaging of the skyrmions, does not possess sufficient resolution to allow the identification of the detailed magnetic structure within the deformed

skyrmions (ref. 8). However, it is possible to correlate the Fresnel images with higher-resolution differential phase contrast images of 5–7 defects, as will be discussed presently.

By comparing the Delaunay triangulation images in Fig. 2b, it is clear that the triangular cells joining each skyrmion location have a lower area in the T_x states, making the overall nearest-neighbour distances shorter than in the P_x states (shown by the colour scale). This difference reinforces the fact that skyrmion creation causes regions of higher skyrmion density (T_x states) that reduce local energetic stability, leading to later relaxation to a P_x state through annihilation of a skyrmion. The fact that these transitions occur spontaneously suggests that the relative energies of the six states are close and that the thermal energy fluctuations of the system are sufficient to overcome the potential energy barriers separating them.

Relative stability and energy landscape

In order to investigate the energetics of the system, the lifetimes of each state over the 1000 frames were measured. Figure 3a shows the lifetime distributions along with the total number of observations of each of the six states, indicating that the P_1/T_1 and P_2/T_2 states were the most commonly observed. Owing to the short-lived nature of the T_x and P_3 states, these transitions may not always be captured individually, but may instead be averaged across the frame duration as previously mentioned. This explanation also suggests why T_x states were not always observed during transitions, since (for example) state lifetimes of 1 ms would contribute only 10% intensity to the final 10 ms frame. It has been established that the system can transition to or from the same P_x state ($P_1-T_1-P_1$ for example). However, if the T_x state was very short-lived, then it is possible that the system could appear to have stayed in the P_x state (P_1-P_1). This “summing” effect might explain some observations of very long lifetimes (around 400 ms) for the P_1 state in Fig. 3a.

The timescale of a magnetic transition between two states, facilitated by the thermal energy of the system, while separated by a simple potential energy barrier, can be deduced from the Néel–Arrhenius equation:

$$\frac{1}{\tau} = v_0(T) e^{-\frac{\Delta E}{kT}} \quad (1)$$

where the lifetime τ of a particular state is the product of the attempt frequency $v_0(T)$ (number of transition attempts per second) and an exponential term containing the Boltzmann factor, which gives the probability of a transition with energy barrier ΔE at temperature T . Using an attempt frequency of 10^9 Hz and kT of 0.022 eV (see Methods for details), energy barriers for the skyrmion creation and annihilation processes were calculated using Eq. 1 (Fig. 3b). The most energetically stable configuration is the P_1 state, corresponding to its relatively long lifetime. Although the less stable P_2 state has 28% more observations than P_1 , this disparity can be understood in view of the fact that the P_2 state is energetically and spatially positioned between the P_1 and P_3 states. Therefore, during a transition from P_1 to P_3 , it is more probable for the system to proceed in multiple lower energy steps via the P_2 state instead of a single step. This is further demonstrated by the individual to/from transition probabilities given in a transition matrix (Fig. 3c) where zero transitions were observed between the P_1 and T_3/P_3 states directly. Figure 3c also demonstrates the symmetry of the transitions, where transitions to or from a particular state had equal probabilities. It should be noted that the T_1 and T_2 states are labelled at the same position in the energy landscape (Fig. 3b). This is because although they are spatially distinct (Fig. 2b), they differ only by a small shift in the skyrmion positions local to the SkCoP and therefore were approximately equally likely to occur (Fig. 3c).

Skyrmion creation and annihilation mechanisms

To better understand the magnetisation distribution within the SkCoH/SkCoP involved in 5–7 defect motion, we performed comparisons with other 5–7 defects not varying in time (i.e., stationary under observation). Figure 4a,b show a static 5–7 defect from a different SkX imaged using the higher spatial resolution technique of differential phase contrast from four-dimensional scanning transmission electron microscopy (4D STEM) (see Methods for details). Figure 4a shows that the SkCoH is quite significantly deformed compared to the lattice skyrmions surrounding it. As we have already noted for our dynamic 5–7 defect, the SkCoH in Fig. 4a also has a greater spatial extent. For the magnitude of the in-plane component of magnetic induction (Fig. 4b), the SkCoH exhibits a significant deformation with clearly defined strip-like regions of in-plane magnetisation connecting it to two neighbouring skyrmions. Additionally, it is possible to identify a stretched core region and some kinking of the magnetisation circulating around it. This situation bears similarity to the structure suggested by the Fresnel images of the SkCoH seen for the dynamic 5–7 defects (Fig. 2).

A Fresnel image of a stable 5–7 defect (from the same SkX domain boundary as the dynamic 5–7 defects) is shown in Fig. 4c, with the intensity across the SkCoH shown in the integrated line profile below. Again, the SkCoH is more spatially extended than hexagonally coordinated lattice skyrmions, but instead of the two distinct central intensity peaks that were observed for the dynamic SkCoH in Fig. 2b, there is a single peak with a shoulder. This pattern indicates that this stationary SkCoH possesses a single core, displaced toward one side. The distance between the two intensity peaks belonging to regular skyrmions in Fig. 4c is approximately 192 nm, whereas this same distance is around 208 nm in the P_x states (see Fig. 2c). This indicates that the SkCoHs involved in 5–7 defect dynamics have a greater lateral spatial extent, possibly giving rise to the additional deformation observed that yields the dumbbell structure. This behaviour may be a contributing factor for the skyrmion creation process through modification of the energy landscape. Comparing the dynamic and stationary SkCoH integrated intensity line profiles (Fig. 2c and Fig. 4c, respectively), the lower relative central peak intensity and greater spatial extent suggests higher variance in the dynamic SkCoH structure.

In order to gain insight into the energy terms that might govern the skyrmion annihilation process we performed a series of micromagnetic simulations of a SkX boundary containing several 5–7 defects (see Supplementary Note 1, and Supplementary Fig. 1). We found that the exchange interactions dominate the total energy density and that there are regions of significantly increased energy density around the SkCoP in the 5–7 defects, because of the locally higher skyrmion density. It follows that the creation of an extra skyrmion creates regions of high skyrmion density (T_x states) with steeper magnetisation gradients, increasing the local exchange energy. Therefore, these states quickly collapse into one of the P_x states via skyrmion annihilation, lowering the skyrmion density.

We propose that an individual SkCoH involved in the observed dynamic processes can split into two separate skyrmions (P_x to T_x transition) through stretching of its form from an elongate structure to a dumbbell structure. Such a deformation is continuous, and consequently, there is no associated change in topology or topological charge. However, at the centre of the dumbbell-like SkCoH structure, significant magnetisation gradients and curvature occur, creating a region of locally high energy density and low energetic stability. Additionally, the magnetisation arrangement in this region is effectively a precursor to the formation of an antiskyrmion. We propose that, through the occurrence of thermal fluctuations, an antiskyrmion arrangement of spins, as depicted in the middle image of Fig. 4d, emerges at some point. This antiskyrmion fulfils topological charge conservation at the precise moment of the SkCoH splitting into two skyrmions. As the resulting two skyrmions move apart, the unstable antiskyrmion is destroyed.

For the case of skyrmion annihilation (T_x to P_x transition), we propose that the reverse mechanism is followed such that the proximity of two merging skyrmions leads to an antiskyrmion, of opposite polarity in this case (Fig. 4e). This antiskyrmion also fulfils topological charge conservation, at the precise moment of skyrmion merging. The reverse mechanism is similar to one suggested for skyrmion lattice inversion during polarity switching of an applied external magnetic field, whereby antiskyrmions are formed at the point of skyrmion core merging¹⁸.

The configurational details of the antiskyrmion transition states were investigated further using micromagnetic simulations. A localised, sub-nanosecond pulsed magnetic field gradient was applied in order to stimulate skyrmion movement (see Supplementary Note 2). The fields act to either pull an elongated skyrmion apart or push two neighbouring skyrmions together (see Supplementary Fig. 2). The resulting transition states resemble those suggested in Fig. 4d,e and demonstrate the apparent inevitability of the creation and subsequent destruction of antiskyrmions during these transitions. This notion of antiskyrmions conserving topological charge during creation or annihilation events has also been studied in dipolar magnets, in which antiskyrmions have a higher stability than that in chiral magnets¹⁹. The thickness of our sample (similar to the skyrmion lattice period, 80 nm) leads us to believe that the mechanism involves the creation and annihilation of antiskyrmions rather than the involvement of Bloch point “zippers”, as discussed in ref. 13, which studied a bulk sample. However, both of these mechanisms involve topological structures that are created and eventually destroyed to fulfil topological charge conservation during transitions.

Recently, a theoretical study using a saddle point search method was used to determine saddle point configurations of skyrmions undergoing duplication and collapse.²⁰ These configurations bear many similarities with the dumbbell-like structures observed and are suggestive of the proposed transition state configurations involving antiskyrmions. It has been shown that, using a 360° domain wall model, skyrmion deformation does not significantly lower the universal skyrmion energy (i.e., energy required to reduce skyrmion radius to zero)²¹. This value should be sufficient to prevent spontaneous skyrmion annihilation processes at the temperatures studied here. However, we propose that thermal fluctuations combined with extreme skyrmion deformation lead to the formation of the

antiskyrmion objects described, providing new energy pathways for skyrmion creation and annihilation that are much lower than the calculated universal skyrmion energy.

Summary and outlook

We observed spontaneous dynamic processes involving the creation and annihilation of individual skyrmions at SkX domain boundaries. Frame-based analysis allowed us to identify key states in the process and to observe variations in the structure of the SkCoH /SkCoP in 5–7 defects that leads to skyrmion creation or annihilation. Naturally, the processes observed are governed by thermal fluctuations and induced exploration of a potential energy landscape, and appeared at first sight not to fulfil the concept of topological charge conservation. However, based on our high-spatial-resolution imaging of other deformed but time-non-varying under observation SkCoH skyrmions and aided by micromagnetic simulations, we have proposed that skyrmions can exhibit extreme deformation, leading to the formation of an antiskyrmion precursor. Through subsequent random local magnetisation fluctuations, the antiskyrmion object may form and subsequently lead to lower energy pathways involving neighbouring skyrmions merging or separating.

Our observations provide evidence of magnetic strain-limited skyrmion energetic stability in lattices, i.e., based on exchange interaction energies. This finding is contrary to many reports of high energetic stability, arising from topological protection for both isolated skyrmions and those in lattices^{21,22,23,24}. Our observations provide the potential for a new method of controlling skyrmion creation and annihilation through engineering SkX boundaries with high magnetic strain, induced via the intentional patterning of magnetic/non-magnetic defects with key dimensions comparable to SkX periodicity. Further time-resolved imaging studies of the extremely deformed skyrmions involved in these dynamic processes may provide new insights into the dynamic transformation processes of topological structures within condensed matter systems.

Methods

Lorentz: Fresnel TEM Imaging

Sections of single-crystal FeGe were extracted from a bulk host crystal using the *in-situ* “Liftout” technique in a focused ion beam-scanning electron microscope (FIB-SEM) instrument (FEI Nova 200 Nanolab). The extracted sections possessed a (110) normal and thickness <100 nm in order to provide sufficient electron transparency. In the TEM (JEOL ARM200cF), the sample was cooled using liquid nitrogen in a Gatan HC3500 specimen holder. For Fresnel mode, defocused imaging of the skyrmion state was performed at a temperature of 253 K with the TEM operating in Low Mag (objective lens OFF mode). Out-of-plane magnetic fields were applied by partially exciting the objective lens. States containing multiple Skyrmion crystal lattices, and therefore boundaries, were induced by starting from a disordered helical state and then by applying and continually increasing the strength of the applied magnetic field up to a value of 510 Oe. Direct filming of the dynamics occurring at skyrmion lattice boundaries was performed using a high-speed, direct illumination, single electron counting 256 × 256 pixel imaging detector (Quantum Detectors Merlin for EM 1R). In these experiments, filming was performed using an exposure time of 10 ms and in continuous read/write mode (i.e., no time gaps between frames), yielding a frame rate of 100 fps.

Lorentz: DPC Imaging

DPC imaging of skyrmions was performed also on a JEOL ARM200cF operating in a custom LM-STEM mode²⁵. An electron probe with semi-convergence angle 415 mrad and full-width-half-maximum of 6 nm was scanned across the sample. 4D STEM acquisition was performed over a 256x256 pixel scan array, 1 ms pixel dwell time (using the same pixelated single electron counting detector as for the Fresnel imaging) to acquire a dataset that was subsequently processed using DPC phase-correlation algorithm in the fpd library²⁶. Isotropic smoothing was applied to the resultant image in order to reduce noise effects and to make clear the features of the distorted skyrmion structure.

Image Analysis

Assignment of each image frame to one of the configurational states was performed by first using the centre of mass of intensity of the skyrmions involved in the lateral motion to create Delaunay triangulation maps. Then, visual inspection and integrated intensity line-profile measurements allowed the identification of the six unique observed states. A Delaunay triangulation of each individual frame was then categorised into one of the six observed states. All analysis of Fresnel images shown in Fig. 2 and Fig. 4c first involved a background subtraction using the “Rolling ball” algorithm. The images shown in Fig. 2 are the result of the summation of many frames in order to significantly reduce influence from the level of statistical noise associated with the limited electron counts in the short movie frames.

Assumptions for relative energy barrier calculations

A precise value of the temperature-dependent attempt frequency $v_0(T)$ in Eq. 1 can be calculated only from detailed information about the minimum energy path taken during transitions²⁷, the exact mechanism of which has not yet been determined for skyrmion merging and splitting. However, it has been reported that the attempt frequency for magnetic skyrmion annihilation in thin films is around 10^9 – 10^{10} Hz²⁸, which is in the range typically reported for other magnetic systems²⁹. A recent study on the entropy-limited topological protection of skyrmions during magnetic phase transitions reports that the attempt frequency may take on values as high as 10^{37} Hz considering high enthalpy–entropy compensation associated with large energy barriers for skyrmion transitions far from equilibrium³⁰. Theoretical studies into the minimum energy pathway of isolated skyrmion collapse also report strong entropy compensation effects under certain conditions, particularly metastable skyrmions far from equilibrium conditions.^{31,32} It was reported that the lower configurational entropy of the saddle point configuration can lead to variations in $v_0(T)$ of up to five orders of magnitude. However, we justify the use of an attempt frequency of 10^9 Hz by noting that the variations in energy barrier height of the observed states are small, reducing entropy compensation effects. Additionally, in the present study we do not have experimental indication of the appropriate modification to $v_0(T)$. Finally, any error in the estimated value of $v_0(T)$ will simply shift the entire energy landscape, leaving the relative barrier heights unchanged.

References

1. Skyrme, T. H. R. A unified field theory of mesons and baryons. *Nucl. Phys.* **31**, (1962).
2. Garaud, J. & Babaev, E. Skyrmionic state and stable half-quantum vortices in chiral p -wave superconductors. *Phys. Rev. B* **86**, 060514 (2012).
3. Fukuda, J. I. & Žumer, S. Quasi-two-dimensional Skyrmion lattices in a chiral nematic liquid crystal. *Nat. Commun.* **2**, (2011).
4. Kiselev, N. S., Bogdanov, A. N., Schäfer, R. & Röller, U. K. Chiral skyrmions in thin magnetic films: New objects for magnetic storage technologies? *J. Phys. D. Appl. Phys.* **44**, 392001 (2011).
5. Fert, A., Reyren, N. & Cros, V. Magnetic skyrmions: Advances in physics and potential applications. *Nat. Rev. Mater.* **2**, (2017).
6. Rößler, U. K., Bogdanov, A. N. & Pfleiderer, C. Spontaneous skyrmion ground states in magnetic metals. *Nature* **442**, 797–801 (2006).
7. Moriya, T. Theory of helical spin structure in itinerant electron systems. *Solid State Commun.* **20**, 291–294 (1976).
8. Yu, X. Z. *et al.* Real-space observation of a two-dimensional skyrmion crystal. *Nature* **465**, 901–904 (2010).
9. Karube, K. *et al.* Robust metastable skyrmions and their triangular-square lattice structural transition in a high-temperature chiral magnet. *Nat. Mater.* **15**, 1237–1242 (2016).
10. Pöllath, S. *et al.* Dynamical Defects in Rotating Magnetic Skyrmion Lattices. *Phys. Rev. Lett.* **118**, (2017).
11. Yu, X. *et al.* Aggregation and collapse dynamics of skyrmions in a non-equilibrium state. *Nat. Phys.* **14**, 832–836 (2018).
12. Jonietz, F. *et al.* Spin transfer torques in MnSi at ultralow current densities. *Science (80-.)* **330**, (2010).
13. Milde, P. *et al.* Unwinding of a skyrmion lattice by magnetic monopoles. *Science (80-.)* **340**, 1076–1080 (2013).
14. Rybakov, F. N., Borisov, A. B., Blügel, S. & Kiselev, N. S. New Type of Stable Particlelike States in Chiral Magnets. *Phys. Rev. Lett.* **115**, (2015).
15. Skowron, S. T., Lebedeva, I. V., Popov, A. M. & Bichoutskaia, E. Energetics of atomic scale structure changes in graphene. *Chem. Soc. Rev.* **44**, 3143–3176 (2015).

16. McGrouther, D. *et al.* Internal structure of hexagonal skyrmion lattices in cubic helimagnets. *New J. Phys.* **18**, (2016).
17. Matsumoto, T. *et al.* Quantum Physics: Direct observation of $\Sigma 7$ domain boundary core structure in magnetic skyrmion lattice. *Sci. Adv.* **2**, (2016).
18. Pierobon, L., Moutafis, C., Li, Y., Löffler, J. F. & Charilaou, M. Collective antiskyrmion-mediated phase transition and defect-induced melting in chiral magnetic films. *Sci. Rep.* **8**, 16675 (2018).
19. Koshibae, W. & Nagaosa, N. Theory of antiskyrmions in magnets. *Nat. Commun.* **7**, 10542 (2016).
20. Müller, G. P. *et al.* Duplication, Collapse, and Escape of Magnetic Skyrmions Revealed Using a Systematic Saddle Point Search Method. *Phys. Rev. Lett.* **121**, (2018).
21. Büttner, F., Lemesh, I. & Beach, G. S. D. Theory of isolated magnetic skyrmions: From fundamentals to room temperature applications. *Sci. Rep.* **8**, 1–12 (2018).
22. Sampaio, J., Cros, V., Rohart, S., Thiaville, A. & Fert, A. Nucleation, stability and current-induced motion of isolated magnetic skyrmions in nanostructures. *Nat. Nanotechnol.* **8**, 839–844 (2013).
23. Leonov, A. O. *et al.* Chiral Surface Twists and Skyrmion Stability in Nanolayers of Cubic Helimagnets. *Phys. Rev. Lett.* **117**, (2016).
24. Oike, H. *et al.* Interplay between topological and thermodynamic stability in a metastable magnetic skyrmion lattice. *Nat. Phys.* **12**, 62–66 (2016).
25. McVitie, S. *et al.* Aberration corrected Lorentz scanning transmission electron microscopy. *Ultramicroscopy* **152**, 57–62 (2015).
26. FPD: Fast pixelated detector data storage, analysis and visualisation. Available at: <https://gitlab.com/fpdpy/fpd/>
27. Legrand, W. *et al.* Room-temperature stabilization of magnetic skyrmions in synthetic antiferromagnets. *Nat. Mater.* 1–23 (2018). doi:10.1038/s41563-019-0468-3
28. Rohart, S., Miltat, J. & Thiaville, A. Path to collapse for an isolated Néel skyrmion. *Phys. Rev. B* **93**, 214412 (2016).
29. Weller, D. & Moser, A. Thermal effect limits in ultrahigh-density magnetic recording. *IEEE Trans. Magn.* **35**, (1999).
30. Wild, J. *et al.* Entropy-limited topological protection of skyrmions. *Sci. Adv.* **3**, (2017).
31. Desplat, L., Suess, D., Kim, J. V. & Stamps, R. L. Thermal stability of metastable magnetic skyrmions: Entropic narrowing and significance of internal eigenmodes. *Phys. Rev. B* **98**, 134407 (2018).
32. Desplat, L., Vogler, C., Kim, J.-V., Stamps, R. L. & Suess, D. Path sampling for collapse rates of metastable magnetic skyrmions and direct comparison with transition state theory. (2019).
33. Vansteenkiste, A. *et al.* The design and verification of MuMax3. *AIP Adv.* **4**, 107133 (2014).
34. Beg, M. *et al.* Ground state search, hysteretic behaviour, and reversal mechanism of skyrmionic textures in confined helimagnetic nanostructures. *Sci. Rep.* **5**, (2015).

Acknowledgements

We would like to thank Y. Kousaka and Y. Togawa of Osaka Prefecture University, Japan for provision of the FeGe single crystals and the EPSRC-JSPS Core to Core grant (EP/M024423/1) and EPSRC/SFI CDT in Photonic Integration and Advanced Data Storage (EPS023321/1) for financially supporting the work.

Author Contributions

F.R.B. performed Fresnel TEM data analysis, carried out micromagnetic simulations and prepared the manuscript. R.J.L. and J.W.J were responsible for preparation of FeGe samples and for acquisition of Fresnel TEM and DPC STEM data sets and analysis. G.W.P. performed advanced processing of the 4D STEM DPC data and assisted with drafting the

manuscript. H.J.M.S and D.M. jointly supervised the work. D.M. was responsible for conception and design of the work and assisted with drafting the manuscript. All authors commented on the manuscript.

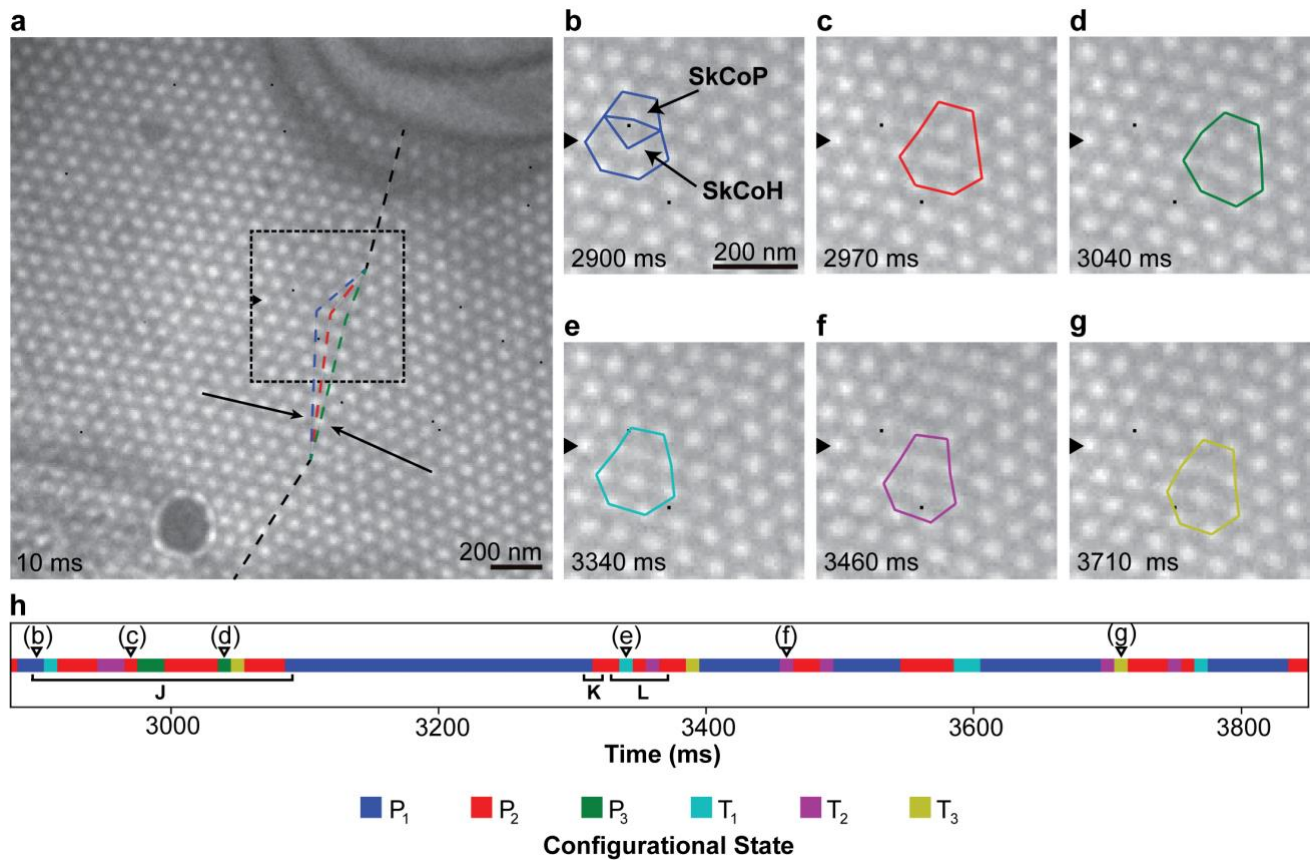


Fig. 1 | Fresnel TEM images of SkX and identification of configurational states. Configurational states in each image coloured according to the bottom key. **a**, Entire region of observed skyrmion lattice, showing the domain boundary with an average misorientation angle of 14° (black dashed line) and principle lattice vectors (arrows). The three coloured dashed lines demonstrate how the domain boundary shifts during transitions between the P_x states and the associated lateral skyrmion motion. **b-g**, Examples of the six configurational states observed, with the time of each frame given in the bottom left corner of each image. The black arrowheads point along the row of skyrmions in which lateral motion was taking place (same position in each image). Skyrmions with seven- and five-fold coordination (SkCoH and SkCoP, respectively) highlighted by the conjoined pentagon and heptagon in **a**. **h**, A portion of the transition data showing the progression of reversible transitions between states shown in **b-g**. The markers in (b)-(g) additionally indicate the time of occurrence of the states shown in **b-g**. Sections J, K and L highlight notable examples of transitions observed: J demonstrates transition reversibility, K indicates a lack of observed T_x state, and L shows a transition via a T_x state back to the original P_x state.

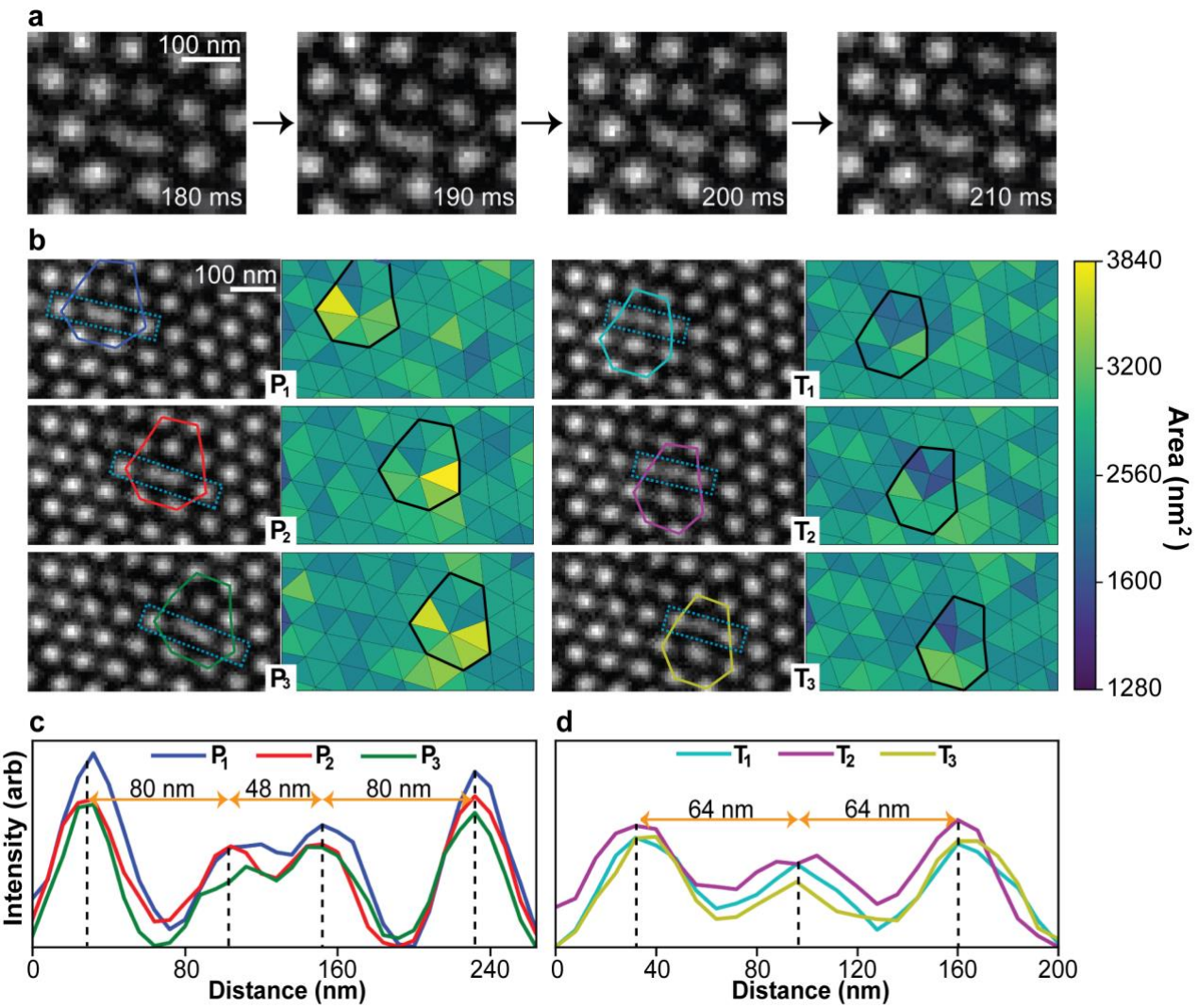


Fig. 2 | Spatial analysis of the six observed configurational states. **a**, Successive frames showing the variation in structure of the SkCoH in the P₁ state with the time of each frame given in the bottom right of each image. **b**, Summed intensity images of each observed state with coloured outlines (same colour key introduced in Fig. 1) around the 5–7 defect (left) and their Delaunay triangulation calculated from the skyrmion geometric centre of mass (right). **c,d**, Integrated line profile plots of the P_x and T_x states respectively, measured across the regions shown in **b** (dashed rectangles). The two outermost peaks are associated with skyrmions of regular regular six-fold coordination. The double inner peak in **c** demonstrates the dumbbell-like structure of each of the SkCoH in the P_x states. The intensity measurements for the T_x states in **d** are poorer statistically than those for the P_x states in **c**, there being rather fewer captured T_x events, which have relatively short lifetimes.

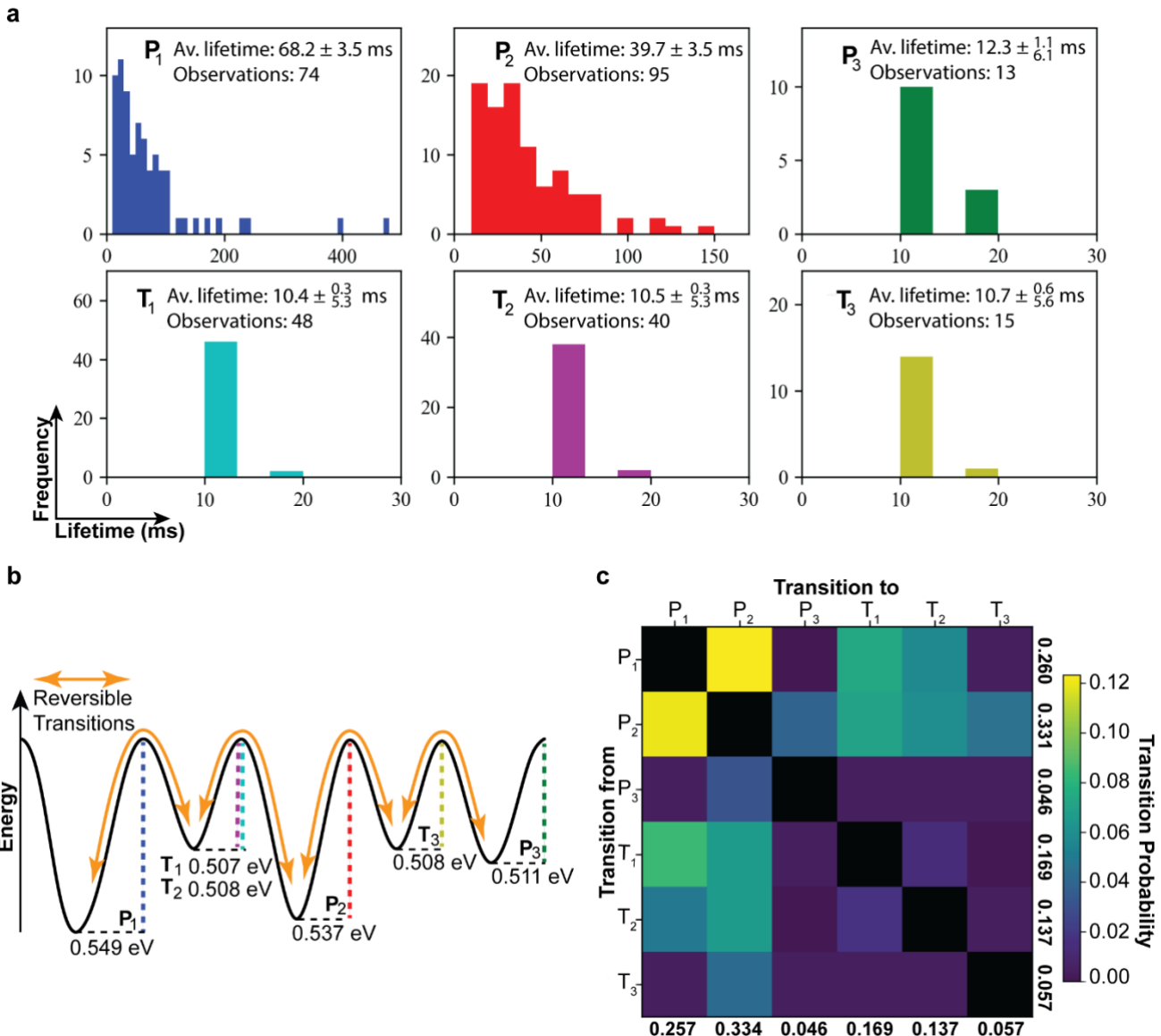


Fig. 3 | Lifetime distributions and associated energy barriers of each state. **a**, Lifetime distributions including the average and number of observations of each state. Half the frame time (5 ms) added to the lower bound in T_x and P_3 lifetime uncertainties due to the short-lived nature of these states not always being captured individually per frame. **b**, Calculated energy barriers using average lifetime with arrows demonstrating the types of observed transitions. **c**, Full transition matrix highlighting the probability of each transition occurring. Bold values at the end of each row/column give the sum of transition probabilities along that row/column.

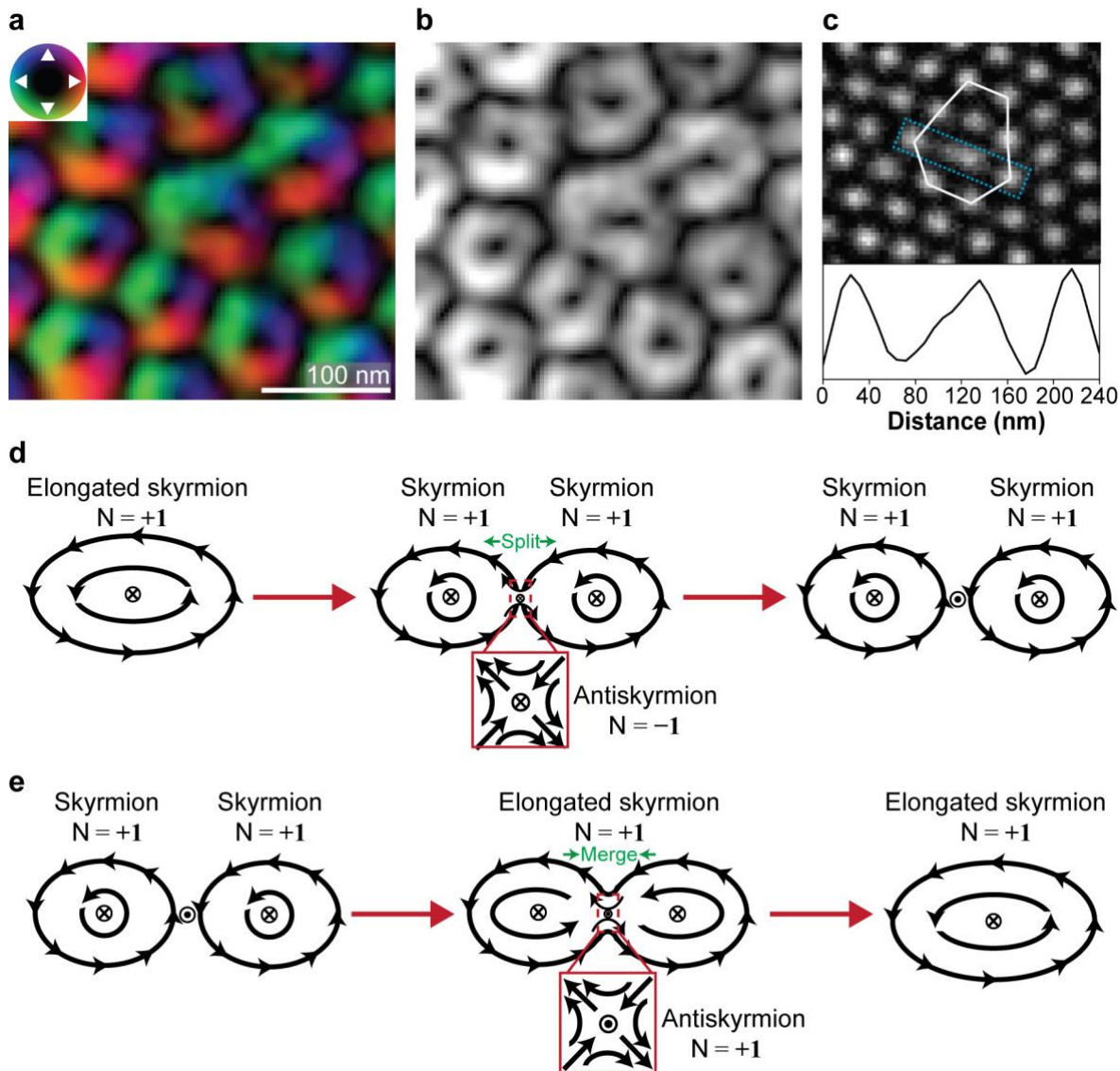


Fig. 4 | Investigation of the SkCoH structure and skyrmion creation and annihilation mechanisms. a,b DPC images of a stable 5–7 defect showing pronounced deformation of the SkCoH structure. Colour in **a** is given by the inset colour wheel which indicates the direction of the in-plane magnetisation. **c**, Fresnel TEM image of a stable 5–7 defect with intensity integrated line profile demonstrating elongated skyrmion structure. **d,e**, Proposed mechanism for skyrmion creation and annihilation respectively, where N gives the topological charge of each structure involved.

Supplementary Materials

Supplementary Note 1: Micromagnetic simulations of skyrmion lattice boundary

Investigation of the energetic stability of 5–7 defects within a domain boundary was performed using finite difference micromagnetic simulations (MuMax3¹) involving a bi-domain skyrmion lattice. Fig. S1 shows the m_z magnetisation component (top) and the energy density plots (averaged over thickness) (middle and bottom) obtained by simulating a thin film of FeGe using periodic boundary conditions in the XY-plane. The simulation parameters were $D = 1.58 \text{ mJ m}^{-2}$, $A = 8.78 \text{ pJ m}^{-1}$ and $M_s = 385 \text{ kA m}^{-1}$ in order to represent the material parameters of FeGe². A perpendicular magnetocrystalline anisotropy constant of 50 kJ m^{-3} was applied to form the initial skyrmion lattice. A cell volume of 3 nm^3 was used, and the sample dimensions were $1284 \text{ nm} \times 648 \text{ nm} \times 12 \text{ nm}$. All simulations were performed with a damping parameter of $\alpha = 0.1$. In order to achieve the bi-domain state shown in Fig. S1, the system was initialised in a randomly magnetised state and allowed to relax into a disordered helical state at zero applied magnetic field. A perpendicular magnetic field of 0.4 T was subsequently applied in order to nucleate skyrmions, and allowed to evolve for a total simulation time of $1 \mu\text{s}$. This length of time was required in order for the randomly distributed skyrmions to form a skyrmion lattice. This resulted in a multi-domain skyrmion lattice. However, the skyrmions were extremely confined and did not exhibit the hexagonal symmetry observed experimentally³. At this point, the perpendicular anisotropy constant was removed, and the external field was reduced to 0.1 T in order to obtain the lattice shown in Fig. S1 after subsequent relaxation. The top image demonstrates the two domain boundaries (dotted lines) which both had a misorientation angle of approximately 21° . The principle lattice vector of each domain is indicated by an arrow. Skyrmion deformation within the domain boundaries is indicated by the expanded SkCoH and contracted SkCoP skyrmions. The middle image shows the total energy density, with the regions of highest energy are found in the inter-skyrmion regions around the SkCoP skyrmions and the regions of lowest energy found local to the SkCoH skyrmions. The bottom three images show the contribution from each of the different energy terms, with exchange and DMI combined because of how MuMax3 calculates the exchange energies. Areas of high exchange energy can be seen in the bottom left image, corresponding to regions of higher skyrmion density and increased instability because of the fact that magnetisation must rotate more quickly in these regions. This pattern can be confirmed by calculating the difference in energy density per cell for skyrmions of five-fold, seven-fold, and regular six-fold coordination. The energy density was summed for the circled regions in Fig. S1 and divided by the number of cells within these regions. The five-fold coordinated skyrmion is $\sim 24\%$ higher in energy than a regular six-fold coordinated skyrmion, and the seven-fold coordinated skyrmion is $\sim 18\%$ lower. These disparities give a relative net energy cost of around 6% for a 5–7 defect compared to two regular skyrmions.

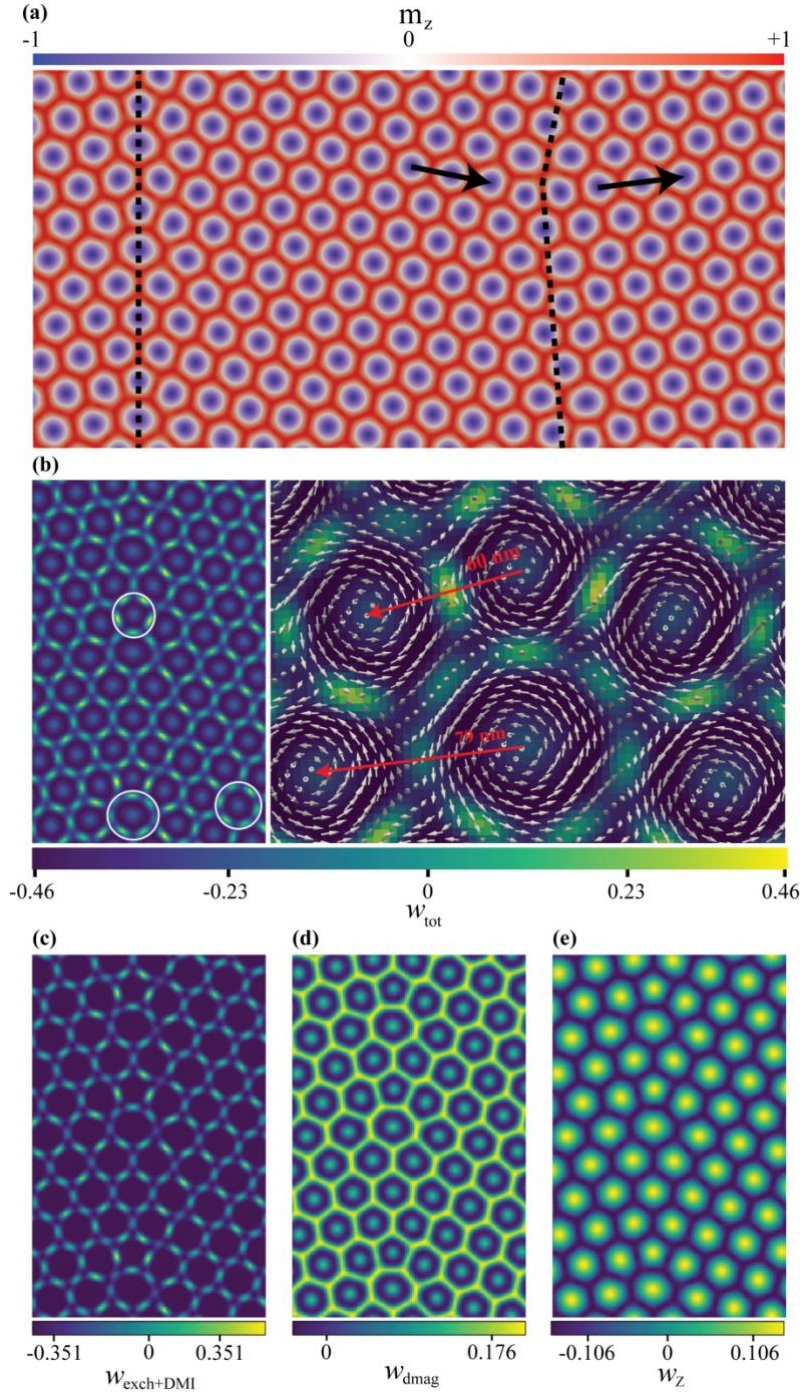


Fig. S1 | Micromagnetic simulations of a skyrmion domain boundary. **a**, Scalar plot of m_z magnetisation of the simulated bi-domain skyrmion lattice. **b**, Scalar plot of total energy density local to a domain boundary (left) with vector plot overlay showing a 5-7 defect (right). All energy densities given in units of A/D^2 . **c-e**, Scalar plots showing exchange+DMI, demagnetising and Zeeman energy densities, respectively, of the same region in **b**.

Supplementary Note 2: Micromagnetic simulations of skyrmion creation/annihilation mechanisms

By using a spatially confined short-duration magnetic field gradient, it was possible to cause the splitting of an elongated skyrmion (Fig. S2a left panel) and the merging of two neighbouring lattice skyrmions (Fig. S2a right panel). Figure S2b, c shows a series of magnetisation snapshots of skyrmion annihilation and creation, respectively. The colour is given by Fig. S2d, where in-plane magnetisation is given by the colour and out-of-plane magnetisation is given by the shade where white points out of the page and black points into the page. The simulation parameters were $D = 1.58 \text{ mJ m}^{-2}$, $A = 8.78 \text{ pJ m}^{-1}$ and $M_s = 385 \text{ kA m}^{-1}$ with zero perpendicular anisotropy. A damping parameter of $\alpha = 0.02$ was used in order to investigate the dynamical aspects of the simulation under study here. A cell volume of 1 nm^3 was used,

and the sample dimensions were $484 \text{ nm} \times 560 \text{ nm} \times 2 \text{ nm}$ for the merging case and $512 \text{ nm} \times 256 \text{ nm} \times 2 \text{ nm}$ for the splitting case.

The merging simulation is shown in Fig. S2a, a very short-pulsed (0.7 ns) magnetic field gradient (25 MT m^{-1}) was localised around a skyrmion in a hexagonal lattice using a two-dimensional gaussian with a standard deviation of 50 nm in the x-direction and 35 nm in the y-direction (shown by the dashed ellipse in the left panel of Fig. S2a). This caused the skyrmion localised under the field gradient to move towards a neighbouring skyrmion and eventually merge. The key points of interest are the appearance, subsequent reduction in size and eventual destruction of the antiskyrmion object shown in the bottom set of panels in Fig. S2b. The antiskyrmion reduces in size, accompanied by a continuous increase in topological charge before being eventually destroyed at $t = 0.684 \text{ ns}$, accompanied by a large discontinuous change in the topological charge (left panel in Fig. S2c). The splitting mechanism is shown in Fig. S2c, again a short-pulsed (0.35 ns) magnetic field gradient of the same strength was localised around the centre of an elongated skyrmion. The standard deviation of the gaussian in this case was 50 nm in both the x- and y-direction. Since the two halves of the skyrmion are being pushed apart by the applied magnetic field gradient, this transition state appears to be slightly different to the one suggested in the main text. However, the appearance and subsequent destruction of an antiskyrmion of opposite polarity to the mechanism in Fig. S2a is clearly shown. Again, the destruction of the antiskyrmion is accompanied by a discontinuous change in topological charge (right panel in Fig. S2c).

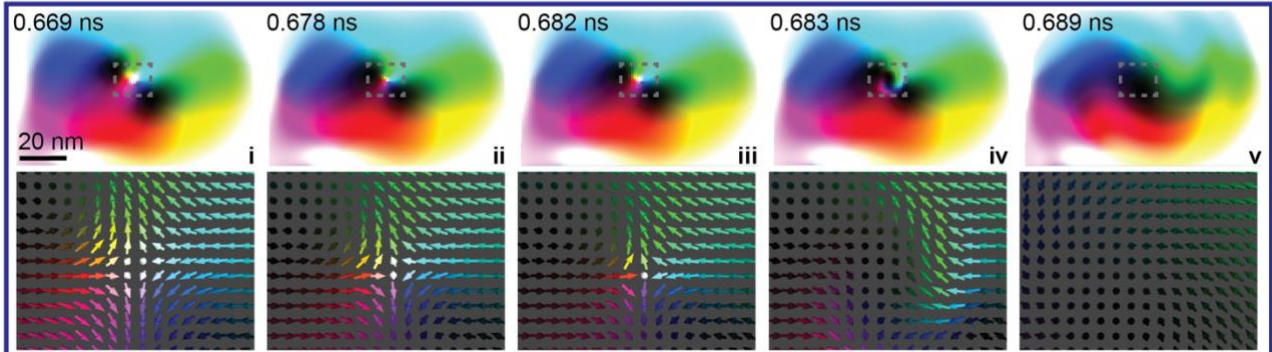
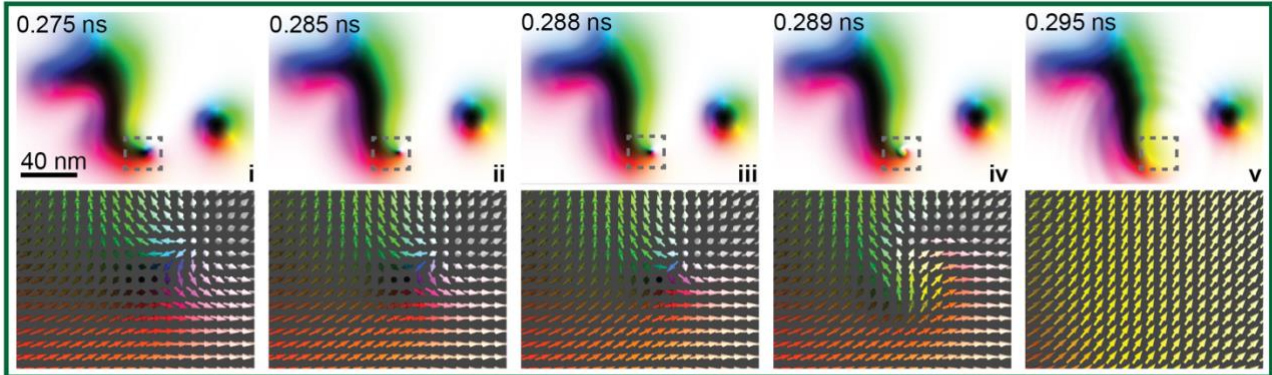
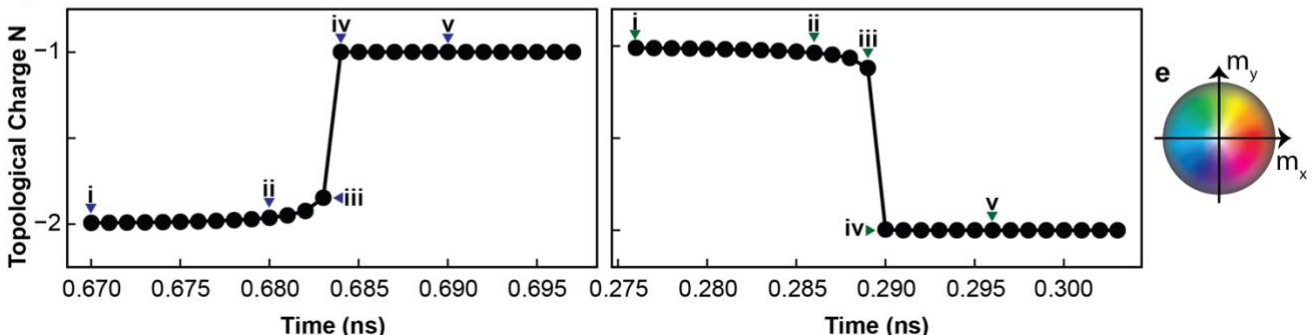
a**b****c****d**

Fig. S2 | Micromagnetic simulations of skyrmion creation/annihilation mechanisms. **a**, Initial states of skyrmion creation (left) and annihilation (right). Dashed ellipses give the first standard deviation of the field-pulse gaussians, with the arrow showing the direction of the magnetic field gradient from positive to negative field. **b,c**, A series of scalar plot snapshots of magnetisation (top) and vector plots of the magnetic field gradient induced skyrmion annihilation/creation mechanisms respectively, colour given by **e**. **d**, Total topological charge as a function of time during the simulation, labels i-v correspond to the panels in **a** and **b**. **d**, Colour wheel for the plots in **b**, **c** where black and white denote magnetisation pointing into and out of the page, respectively.

Supplementary Video

Fresnel TEM video containing 1000 frames with a frame acquisition time of 10 ms and a total time of 10 s. Video shows the spontaneous merging and separation of skyrmions across a skyrmion domain boundary.

1. Vansteenkiste, A. *et al.* The design and verification of MuMax3. *AIP Adv.* **4**, 107133 (2014).
2. Beg, M. *et al.* Ground state search, hysteretic behaviour, and reversal mechanism of skyrmionic textures in confined helimagnetic nanostructures. *Sci. Rep.* **5**, (2015).
3. McGrouther, D. *et al.* Internal structure of hexagonal skyrmion lattices in cubic helimagnets. *New J. Phys.* **18**, (2016).